Front. Mech. Eng. 2020, 15(1): 24–42
https://doi.org/10.1007/s11465-019-0558-6

RESEARCH ARTICLE

Jinghua XU, Tiantian WANG, Qianyong CHEN, Shuyou ZHANG, Jianrong TAN

Performance design of a cryogenic air separation unit for variable working conditions using the lumped parameter model

Abstract Large-scale cryogenic air separation units (ASUs), which are widely used in global petrochemical and semiconductor industries, are being developed with high operating elasticity under variable working conditions. Different from discrete processes in traditional machinery manufacturing, the ASU process is continuous and involves the compression, adsorption, cooling, condensation, liquefaction, evaporation, and distillation of multiple streams. This feature indicates that thousands of technical parameters in adsorption, heat transfer, and distillation processes are correlated and merged into a large-scale complex system. A lumped parameter model (LPM) of ASU is proposed by lumping the main factors together and simplifying the secondary ones to achieve accurate and fast performance design. On the basis of material and energy conservation laws, the piecewise-lumped parameters are extracted under variable working conditions by using LPM. Takagi–Sugeno (T–S) fuzzy interval detection is recursively utilized to determine whether the critical point is detected or not by using different thresholds. Compared with the traditional method, LPM is particularly suitable for "rough first then precise" modeling by expanding the feasible domain using fuzzy intervals. With LPM, the performance of the air compressor, molecular sieve adsorber, turbo expander, main plate-fin heat exchangers, and packing column of a 100000 Nm^3 O_2/h large-scale ASU is enhanced to adapt to variable working conditions. The designed value of net power consumption per unit of oxygen production (kW/(Nm^3 O_2)) is reduced by 6.45%.

Received January 25, 2019; accepted July 3, 2019

Jinghua XU, Tiantian WANG, Qianyong CHEN, Shuyou ZHANG (✉), Jianrong TAN
State Key Laboratory of Fluid Power and Mechatronic Systems, Zhejiang University, Hangzhou 310027, China; Key Laboratory of Advanced Manufacturing Technology of Zhejiang Province, School of Mechanical Engineering, Zhejiang University, Hangzhou 310027, China
E-mail: zsy@zju.edu.cn

Keywords performance design, air separation unit (ASU), lumped parameter model (LPM), variable working conditions, T–S fuzzy interval detection

1 Introduction

Industrial gases, such as oxygen (O_2), nitrogen (N_2), and argon (Ar), are important feedstock or energy sources in petrochemical, aerospace, thermal power, ferrous metallurgy, and other modern industries. Industrial gases are usually produced by air separation units (ASUs) [1]. ASUs are used to separate atmospheric air into its initial components, which are usually O_2, N_2, Ar, and other inert gases, by using various air separation processes, such as cryogenic distillation, membrane adsorption, pressure swing adsorption, and vacuum pressure swing adsorption [2]. The most effective method to produce large quantities of high-purity industrial gases is cryogenic air separation, which is a capital and energy-intensive process [3]. ASUs are being developed with large capacity, high efficiency, high automation, and high reliability to meet increasing industrial requirements. Different from discrete processes in traditional machinery manufacturing, the ASU process is continuous and involves the compression, adsorption, cooling, condensation, liquefaction, evaporation, and distillation of multiple streams. This feature means that thousands of technical parameters in adsorption, heat transfer, and distillation processes are correlated and merged into a large-scale complex system (LSCS). The ASU field involves multilateral knowledge from various areas, such as thermal science, electromechanical dynamics, hydromechatronics, automation control, and physical chemistry. Improving the independent design level, innovation, and international competitiveness of reconfigurable mechanical products is important [4]. Therefore, how to achieve accurate and fast performance design of ASUs is a major challenge for the academia.

In theoretical research on cryogenic ASUs, Huang et al.

[5] conducted theoretical research on cryogenic ASUs and reported that such ASUs fluctuate in variable working conditions to respond to changing product demands; they proposed a nonlinear model predictive control based on rigorous dynamic models for cryogenic ASUs to overcome this problem. Kansha et al. [6] introduced a novel cryogenic air separation process based on self-heat recuperation; the energy consumption of the proposed process is 36% lower than that of the conventional cryogenic air separation process. Fu et al. [7] developed a complete equation-oriented model that can be used to solve particular issues in cryogenic air separation, namely, thermodynamic parameter estimation, process analysis with heat-coupling design, and process optimization with varying load demands.

In the experimental research on cryogenic ASUs, Aneke and Wang [8] conducted on cryogenic ASUs, they investigated the potential of improving the energy efficiency of a conventional cryogenic ASU by using binary heat recovery cycles through modeling and simulation. The simulation results showed that the net power consumption of the conventional cryogenic ASU is reduced. Cao et al. [9] proposed a full-order stage-wise model for distillation columns in ASUs in consideration of key process phenomena. The simulation results showed that the thermal integration between feed and product flows captured in the primary heat exchanger is the key to determining the behavior of ASUs accurately. Ebrahimi and Ziabasharhagh [10] used liquefied natural gas cold energy for a cryogenic ASU to improve the performance of this cycle. This integration reduces the power demand and initial capital cost of ASU by 8.04% and 17.5%, respectively.

In optimization research on cryogenic ASUs, Rizk et al. [11] simulated three types of distillation and calculated the exergy in the different parts. The results showed that the exergy efficiency of a double diabatic column is 23% higher than that of conventional columns. Tong et al. [12] proposed a combined variable oxygen supply method for a cryogenic ASU to reduce energy consumption. The results showed that the total energy efficiency of the ASU is increased by 11%–31%. Jin et al. [13] used control optimization aided by the dynamic exergy method to implement energy-efficient operations for cryogenic ASUs. Dynamic process real-time optimization system operation is expected to achieve significant energy saving.

With the increasing demands for industrial gases, traditional small-scale ASUs cannot easily meet the requirements of industries. The size of each device in ASUs must be increased to obtain the optimal efficiency of large-scale ASUs, and thousands of technical parameters need to be integrated into adsorption, heat transfer, and distillation processes. On the basis of our previous work [14–17], we develop a lumped parameter model (LPM) method to achieve accurate and fast performance design of large-scale ASUs.

2 Air separation process of large-scale cryogenic ASUs

Cryogenic ASUs involve two main processes, namely, external (Fig. 1) and internal (Fig. 2) compression. The main difference between them is that the liquid oxygen pump (Label 13 in Fig. 2) between the main plate-fin heat exchangers (PFHEs) (Label 12 in Fig. 2) and the main condenser evaporator (Label 15 in Fig. 2) is further pressurized for internal compression. Compared with the external compression process, the internal compression process has better safety, higher liquid gas output, smaller floor space, and easier maintenance; however, the cost is also high. The internal compression process is the optimal choice for large-scale ASUs, and the process flow is more complicated than that of external compression.

ASUs have many kinds of refrigeration cycles, but most of them are based on Linde and Claude cycles [18]. The Linde cycle involves throttling expansion refrigeration. The Claude cycle still involves throttling expansion, and a part of the gas undergoes isentropic expansion in the turbo expander (TE) (Label 11 in Fig. 1). When the gas is subjected to isentropic expansion, the temperature drop is larger than that during throttling expansion. Part of the compression work can be recovered in isentropic expansion; thus, it is more economical than throttling expansion. Therefore, the expansion process is increasingly used to generate cold energy with high energy efficiency.

As shown in Fig. 1, a cryogenic ASU mainly consists of an air compressor (AC), a molecular sieve adsorber (MSA) (Label 8 in Fig. 1), a TE (Label 11 in Fig. 1), PFHEs (Label 12 in Fig. 1) and a packing column (PC) (lower and upper columns (LC and UC), Labels 13 and 15 in Fig. 1). Atmospheric air (Label 1 in Fig. 1) passes through AC (Label 3 in Fig. 1) and the air-cooling column (Label 5 in Fig. 1) then enters MSA to remove impurities. After adsorption, the atmospheric air becomes high-pressure air (HPA). HPA diverges into two streams, namely, main air (MA) and turbo expander air (TA). After being treated by the main PFHEs, MA and TA enter the LC. Air separation primarily occurs in two PCs, which are high-pressure LC (Label 13 in Fig. 1) and low-pressure UC (Label 15 in Fig. 1); the main condenser evaporator (Label 14 in Fig. 1) is in the middle. Gaseous oxygen (GOX), liquid oxygen (LOX), gaseous nitrogen (GAN), liquid nitrogen (LIN), and gaseous argon (GAR) are the five products generated by condensation and evaporation in the PCs. These streams are sent to the LC after being cooled and fed to the UC for further distillation and production of GAN at the top and LOX at the bottom. Most of LOX is withdrawn as a final product, and the remainder is pumped and vaporized into GOX [7]. Crude nitrogen is extracted from the main PFHEs as a reflux to improve the cooling capacity. GAR can be obtained by condensation and evaporation using the crude argon columns (Labels 17 and 19 in Fig. 1) and pure argon column (Label 22 in Fig. 1).

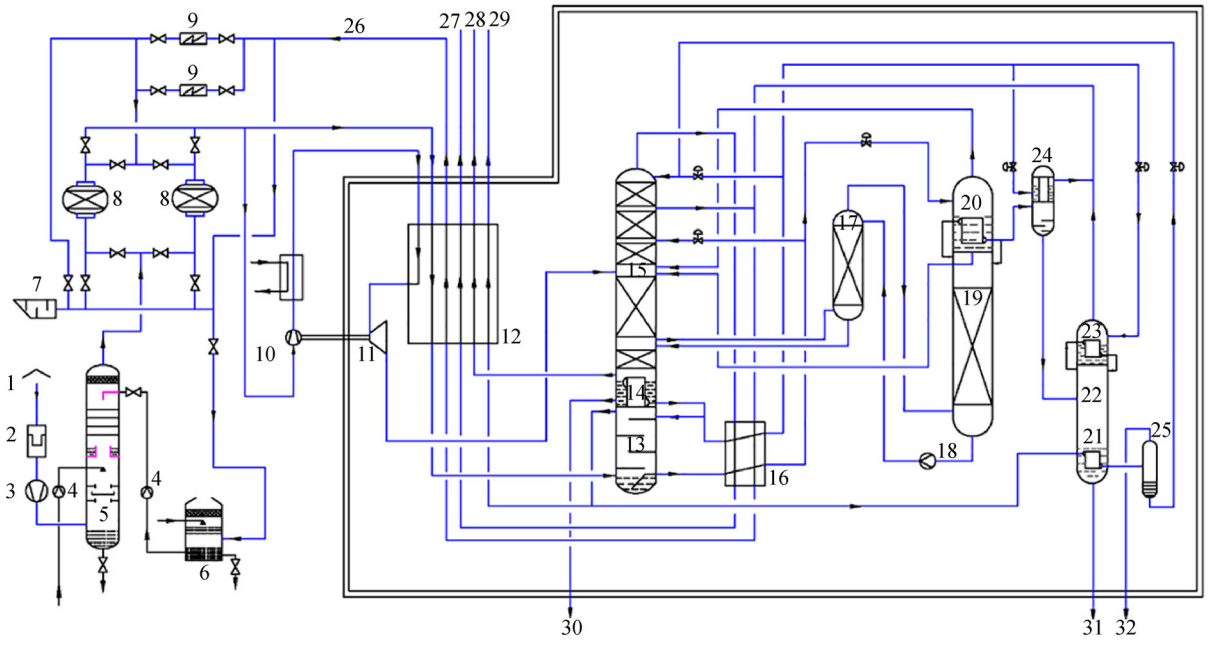

1–Atmospheric air; 2–Self-cleaning air filter; 3–AC; 4–Water pump; 5–Air-cooling column; 6–Water-cooling column; 7–Silencer; 8–MSA; 9–Electric heater; 10–Supercharger; 11–TE; 12–Main PFHEs; 13–LC; 14–Main condenser evaporator; 15–UC; 16–Subcooler; 17–Crude argon column I; 18–Liquid argon pump; 19–Crude argon column II; 20–Crude argon evaporator condenser;21–Pure argon evaporator; 22–Pure argon column; 23–Pure argon condenser; 24–Crude argon liquefier; 25–Liquid argon (LAR) balancer; 26–Crude nitrogen; 27–GAN; 28–GOX; 29–Compressed nitrogen; 30–LOX; 31–LAR; 32–GAN.

Fig. 1 Typical external compression cryogenic air separation process.

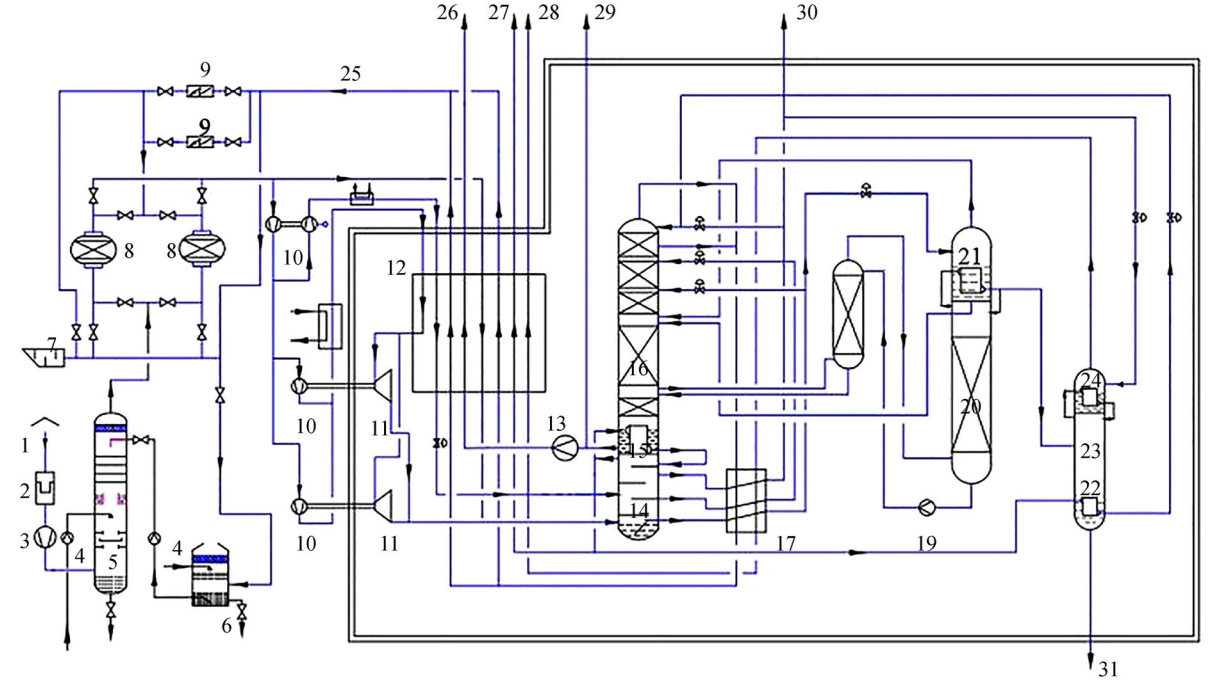

1–Atmospheric air; 2–Self-cleaning air filter; 3–AC; 4–Water pump; 5–Air cooling column; 6–Water-cooling column; 7–Silencer; 8–MSA; 9–Electric heater; 10–Supercharger; 11–TE; 12–Main PFHEs; 13–Liquid oxygen pump; 14–LC; 15–Main condenser evaporator; 16–UC; 17–Subcooler; 18–Crude argon column I; 19–Liquid argon pump; 20–Crude argon column II; 21–Crude argon evaporator condenser; 22–Pure argon evaporator; 23–Pure argon column; 24–Pure argon condenser; 25–Crude nitrogen; 26–GOX; 27–Compressed nitrogen; 28–GAN; 29–LOX; 30–LIN; 31–LAR.

Fig. 2 Typical internal compression cryogenic air separation process.

As indicated in Figs. 1 and 2, the feedstock of ASUs includes various flowing streams, which can be air, water, cold streams, and hot streams. The compressor unit adopts AC and a supercharger, and the power originates from the steam turbine to improve the efficiency of ASU and achieve feedstock conservation. The steam turbine is a dual output shaft. One end directly drives the AC, and the other end drives the supercharger via the gearbox. This form of work is called "one drives two." This method can effectively utilize waste steam to drive the steam turbine and achieve feedstock conservation. It is meaningful for industries with massive waste heat.

3 LPM for large-scale cryogenic ASUs

3.1 Design challenges in large-scale cryogenic ASUs

In the flowing domains of large-scale cryogenic ASUs, with the increase in flow rate, a slight deviation in the predicted properties of fluid causes a significant error. For large-scale cryogenic ASUs, pressure and temperature may cause a supercritical status. A supercritical fluid (SCF) is any substance at a temperature and pressure above its critical point, where distinct liquid and gas phases do not exist. When approaching the critical point, a slight change in pressure or temperature leads to a massive change in the physical properties of SCFs. Although the physical properties and applications of SCFs in supercritical technology differ, the physical properties of the key areas are similar.

Large-scale ASUs bring many problems, including high temperature and high pressure, inside different devices, such as AC, TE, and main PFHEs. This condition poses a great challenge to the prediction of fluid physical properties in ASUs. For example, in the main PFHEs, most of the cold and hot fluids are above the critical point, and accurate prediction of their working parameters has an important influence on the heat exchange performance of the heat exchanger. SCF properties in the design of PFHEs are becoming increasingly popular and considerably affect the performance of PFHEs. These properties provide an important reference for reducing exergy destruction and lead to effective heat utilization, especially at low-temperature-level waste heat [19]. Many studies have been conducted on supercritical problems. Son and Park [20] developed a new correlation for predicting the heat transfer coefficient of supercritical CO_2 in the process of tube cooling. Lisboa et al. [21] used three models (standard k–ε, re-normalization group k–ε, and k–ω) to model the flow and heat transfer of SCF under high pressure. Negoescu et al. [22] studied the heat transfer behavior of supercritical nitrogen to achieve the ultimate goal of cryogenic process optimization design. With the increase in heat flux, the heat transfer process changes from normal mode to deteriorating mode. Avili et al. [23] investigated the effect of liquid redistribution on wall flow reduction in the PCs of cryogenic distillation. The liquid redistributor is associated with the characteristics of SCFs. When the diameter of the packed column is less than 0.05 m, the liquid should be redistributed with a smaller spacing than that in a large packed column. Raman et al. [24] believed that the supercritical state can be divided into regions with similar liquid and vapor properties by a widow line. They determined the widow line of oxygen consisting of the second residue of the thermodynamic response function in the supercritical region by atomic theory. Therefore, this study proposes a method based on Takagi–Sugeno (T–S) fuzzy interval detection to calculate working parameters. Many physical property calculation methods are based on Helmholtz energy equations [25] and the Grüneisen parameter test method [26], which can qualitatively predict the special trend of thermal properties.

3.2 T–S fuzzy interval detection to judge the critical point of ASU

The key to the design for variable working conditions is to determine whether the critical point is detected or not. Saha and Sandilya [27] proposed a dynamic LPM of an injection cooling system for liquid subcooling. Liu and Xu [28] studied a neuron proportional–integral–derivative (PID) controller that can adjust parameters according to the changes in the controlled object and input reference signal. The results showed that the proposed PID controller has high control precision. To determine whether the state is in a normal working condition or not, T–S fuzzy interval detection is used to predict working parameters. The main idea is to obtain function approximation from a set of finite measurement data by using the optimality criterion to minimize the estimation error.

The traditional method for the variable working condition design of ASUs using a predefined uniform threshold cannot detect the critical operating condition adaptively. Therefore, T–S fuzzy interval detection is recursively used to judge whether the critical point is detected or not by using different thresholds.

For ASUs under normal working conditions, n known states $S_k = \{S_k^{(1)}, S_k^{(2)}, ..., S_k^{(n)}\}$ exist. A typical fuzzy model is given as [29]

$$\text{if } x_1 \text{ is } S_k^{(1)}, x_2 \text{ is } S_k^{(2)}, \ ..., \text{ and } x_n \text{ is } S_k^{(n)},$$

$$\text{then } y_i = f_i(\boldsymbol{x}),\ i = 1, 2, ..., n, \tag{1}$$

where $\boldsymbol{x}^{\mathrm{T}} = [x_1, x_2, ..., x_n]$ denotes the input or variables in the premise, y_i is the output of the model, and S_k is the known state.

With each variable in premise x_i, f_i fuzzy sets $(S_k^{(1)}, S_k^{(2)}, ..., S_k^{(n)})$ are connected, and each fuzzy set $S_k^{(i)}$

is associated with a real valued function $g_i(x_i)$ that produces the membership grade of x_i with respect to the fuzzy set $S_k^{(i)}$ [30]. The fuzzy membership function $g_i(x_i)$ of the ith judgement can be obtained with Eq. (2):

$$g_i(x_i) = \frac{1}{1 + \left|\frac{x_i - c_i}{a_i}\right|^{2b_i}},\ i = 1, 2, ..., n, \tag{2}$$

where a_i, b_i, and c_i are the parameter sets of the shape-changing degree of the membership function, a_i, b_i, and $c_i \in [0, 1]$, and $g_i(x_i) \in (0, 1]$.

The final output y_f of the T–S fuzzy model can be written as Eq. (3):

$$y_f(\boldsymbol{x}) = \sum_{i=1}^{n} g_i(x_i) f_i(\boldsymbol{x}), \tag{3}$$

where $\sum_{i=1}^{n} g_i(x_i) = 1$.

For n-dimension known data, the fuzzy approximation error λ_i of the ith judgement is proposed to minimize the error sequence:

$$\lambda = \min\{\lambda_1, \lambda_2, ..., \lambda_n\}, \tag{4}$$

where $\lambda_i = y_i - y_f(x_i)$, $i = 1, 2, ..., n$.

Equation (4) can be further converted into an optimization model with a minimum two-norm solution and solved by linear programming.

Its algorithm flow is shown in Fig. 3.

4 LPM of the adsorption process

The adsorption process consists of two main devices: The AC that is used to compress air and provide flowing power and the MSA that is used to remove impurities in the compressed air. For AC, the large size of ASU and the total amount of compressed air per unit time increase, which is a challenge to the structure design and service life of AC. For MSA, it can be formally divided into horizontal and vertical radial types. Compared with horizontal MSA, vertical radial MSA covers a smaller area and is widely used, and it is easy to maintain in the future. LPMs of AC and MSA are established for variable working conditions.

4.1 LPM of AC for variable working conditions

The main power source of the compressor is electric energy, which accounts for a large part of the power consumption in

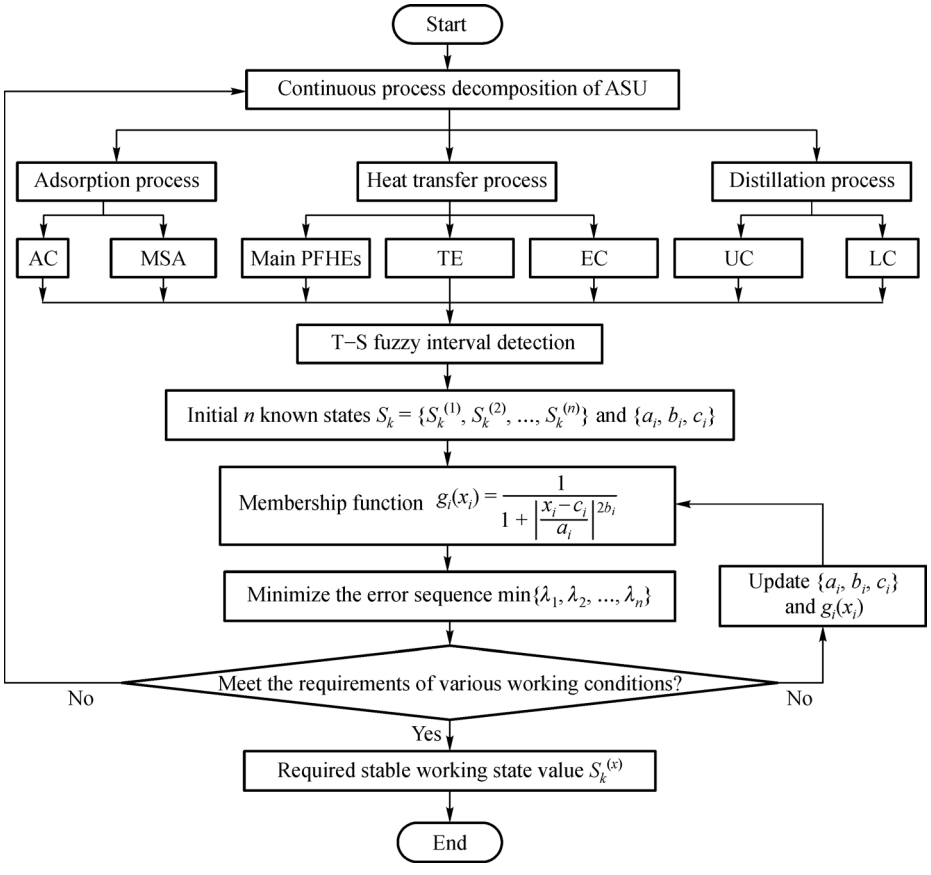

Fig. 3 T–S fuzzy interval detection to judge the critical point of ASU.

ASU. AC is the power source dynamic equipment in ASU. According to the classification of the compressor structure, it can be divided into centrifugal and axial flow compressors. An "axial-centrifugal compressor" is used with a large inlet flow rate, high efficiency, wide working range, and high reliability. The first section adopts an axial flow compressor, which has the characteristics of large flow rate, short air flow, and small resistance loss; the second section adopts a centrifugal compressor, which has the characteristics of high pressure, high efficiency, and smooth operation.

To meet variable working conditions, the AC should be precisely controlled for avoiding surge and stonewall [31,32]. Torrisi et al. [33] used a model predictive control technique to address process and anti-surge control and achieve the desired pressure ratio and surge distance for industrial centrifugal compression systems with nonlinear dynamics. Gravdahl et al. [34] used the drive itself for surge control. Doing so eliminates the need for additional actuators and has the potential to achieve energy-efficient operation. Boinov et al. [35] presented a method for active surge suppression of a centrifugal compressor by means of the speed control of the electrical drive. If the internal pressure of the AC is about 110%–120% of the design pressure, a surge phenomenon will arise; meanwhile, about 60% of the design pressure will cause a stonewall phenomenon. The pressure flow characteristic curve can be obtained through a surge test under different conditions (i.e., low, medium, and high flows). The surge point, surge boundary line, or surge area can be determined according to the characteristic curve to avoid the surge phenomenon.

To meet the requirements of large flow rate, high pressure ratio, and high efficiency, a 100000 Nm^3 O_2/h large-scale ASU compression unit is designed to adopt an "axial–centrifugal" coaxial structure. The AC unit uses the "one drives two" process via intelligent interlock control. Figure 4(a) shows an AC, Fig. 4(b) shows a digital mockup (DMU) of the AC, Fig. 4(c) shows the CFD simulation of the work flow in the AC, and Fig. 4(d) presents the air temperature change in the AC.

The LPM of AC is as follows. The large-scale ASU requires a high air mass flow rate and has high requirements on AC efficiency. The compressor's isentropic efficiency η_{AC} is the ratio of the isentropic power of the compressor to the actual power required to compress the working medium. It can be determined by Eqs. (5)–(7). The working parameters, such as C_p, T_i, and T_o, can be obtained with the T–S model.

$$\eta_{AC} = \dot{m}_{air}(h_o - h_i)/P_s, \tag{5}$$

where η_{AC} is the isentropic efficiency of the compressor, $\dot{m}_{air}$ is the mass flow rate of atmospheric air (unit: kg/s), h_o is the total specific enthalpy of the isentropic process at the outlet of the compressor (unit: J/kg), h_i is the total specific enthalpy of the isentropic process at the inlet of the compressor (unit:

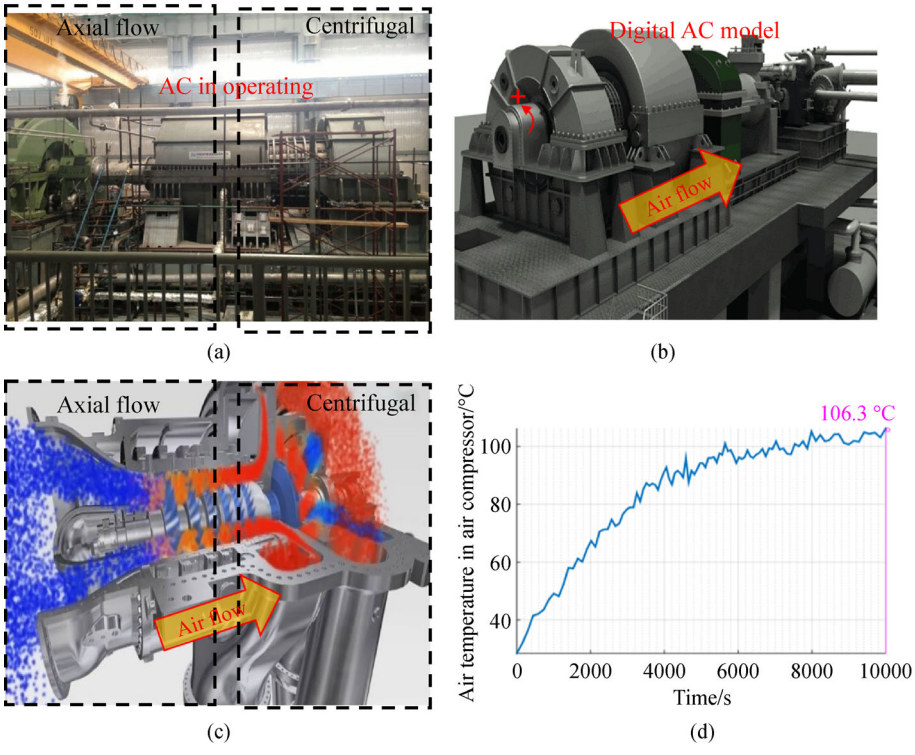

Fig. 4 AC. (a) AC in a factory; (b) digital mockup of the AC; (c) CFD simulation of the work flow in the AC; (d) air temperature change in the AC.

J/kg), and P_s is the shaft power of AC (unit: kW).

$$h_i = C_p T_i, \tag{6}$$

$$h_o = C_p T_o, \tag{7}$$

where T_i is the inlet temperature of the compressor (unit: K) and T_o is the outlet temperature of the compressor (unit: K).

As shown in Figs. 1 and 2, after passing through the AC, the air changes into high-pressure gas and enters MSA. The pressure of the high-pressure air depends on the compression ratio of the compressor.

$$P_{MSA,i} = P_{AC,o} = P_{AC,i}\gamma, \tag{8}$$

where $P_{MSA,i}$ is the inlet pressure of the fluid at MSA (unit: MPa), $P_{AC,o}$ is the outlet pressure of the fluid at AC (unit: MPa), $P_{AC,i}$ is the inlet pressure of the fluid at AC (unit: MPa), and γ is the compression ratio of AC, $\gamma \in [1, +\infty)$.

4.2 LPM of MSA for variable working conditions

The air purification system is crucial for air purification and pretreatment in large-scale cryogenic ASUs. The energy consumption of an air purification system accounts for about 16% of the total energy consumption of an ASU. This system is used to clean water, carbon dioxide, and hydrocarbon C_xH_y (acetylene, etc.) in air to prevent low-temperature equipment from blocking or even exploding and ensure the long-term safety and reliability of the ASU [36]. The main adsorbents are zeolite, alumina, silica gel, and molecular sieve.

MSA can be divided into three types according to different flow forms, which are vertical axial, horizontal bed, and vertical radial flows. Vertical axial flow MSA is mainly used in small-scale ASUs (below 20000 Nm^3 O_2/h). Horizontal bed MSA is primarily utilized in medium-scale ASUs (between 20000 and 45000 Nm^3 O_2/h). Vertical radial flow MSA is mainly adopted in large-scale ASUs (above 45000 Nm^3 O_2/h). A vertical radial flow MSA generally occupies a small floor space. The flow resistance through the adsorbent is decreased, and the airflow is easier to distribute. An air purification system has two large vertical radial flow MSAs. One is for adsorption, and another is for regeneration. When the one for adsorption is saturated, the regeneration absorber is switched to work alternately and periodically. The regeneration process removes impurities in the sorbent to restore the absorbability of the adsorbent. It can have a long duration, automatic adsorption cycle switching, and no impact switching control technology. Figure 5(a) shows two vertical radial flow MSAs; and Fig. 5(b) shows the simulation process of MSAs.

The relationship between the resistance of vertical radial flow MSA and fluid mass flow rate is established based on the following simplifying assumptions:

(1) Assuming that the air is incompressible, the air density inside the MSA is constant.

(2) Assuming that the air mass flow rate is constant in the internal flow of MSA, the amount of air adsorbed is ignored.

(3) Assuming that the adsorbent is a homogeneous continuous medium, the physical parameters and adsorption capacity do not vary with temperature and pressure.

(4) Assuming that no concentration and temperature gradients exist in MSA, the pressure loss only exists in the direction of airflow.

The LPM of MSA is as follows. The main factor for evaluating the performance of MSA is the pressure drop of molecular sieves. The pressure drop of MSA can be calculated with Eqs. (9)–(12). It is mainly related to the mass flow rate, density, and dynamic viscosity of fluids. These parameters can be calculated by LPM. The air from MSA enters the main PFHEs and TE. In this process, the pressure of the fluid is essential. The outlet pressure of the fluid at MSA can be obtained with Eq. (9):

$$P_{MSA,o} = P_{MSA,i} - \Delta P_{MSA}, \tag{9}$$

where $P_{MSA,o}$ is the outlet pressure of the fluid at MSA (unit: MPa) and ΔP_{MSA} is the pressure drop of MSA (unit: MPa).

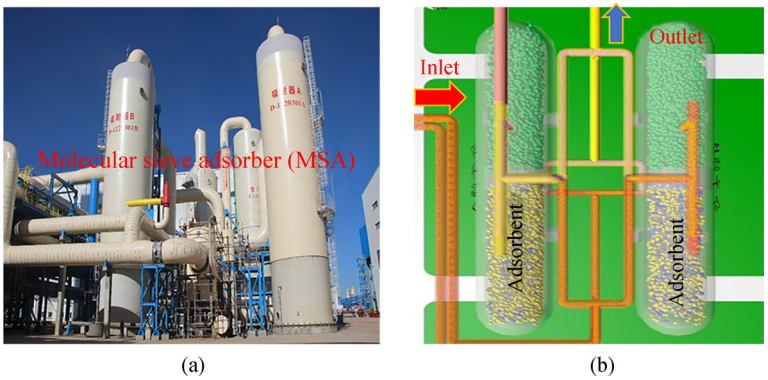

(a) (b)

Fig. 5 MSA. (a) Two vertical radial flow MSAs; (b) simulation process of MSAs.

The mathematical expression of the pressure drop of MSA can be obtained as

$$\Delta P_{\mathrm{MSA}}/H = k_1 u\mu(1-\varepsilon)^2/\varepsilon^2 + k_2\rho u^2(1-\varepsilon)/(d\varepsilon^3), \quad (10)$$

where H is the height of MSA (unit: m), k_1 and k_2 are constants, μ is dynamic viscosity (unit: Pa·s), ε is porosity, d is the bore diameter (unit: m), and ρ is the fluid density (unit: kg/m^3).

$$\dot{m}_{\mathrm{air}} = \rho u A_{\mathrm{f}}, \quad (11)$$

where $\dot{m}$ is the fluid mass flow rate (unit: kg/s), A_{f} is the total area of the void hole through which the fluid flows (unit: m^2), and u is the fluid flow speed (unit: m/s).

According to Eq. (11), Eq. (10) can be rewritten as follows:

$$\Delta P_{\mathrm{MSA}} = \dot{m}_{\mathrm{air}} k_1 \mu(1-\varepsilon)^2/(\rho A_{\mathrm{f}}\varepsilon^2) + \dot{m}_{\mathrm{air}}^2 k_2(1-\varepsilon)/(\rho d A_{\mathrm{f}}^2\varepsilon^3). \quad (12)$$

Equation (12) indicates that ΔP_{MSA} is positively related to $\dot{m}$. As $\dot{m}$ increases, ΔP_{MSA} increases faster, and $P_{\mathrm{MSA,o}}$ decreases.

5 LPM of the heat transfer process

The heat transfer process consists of two main devices: TE and PFHEs. The TE is used to generate cold energy for the ASU, and PFHEs are devices for the heat exchange of cold and hot fluids. Multi-stream PFHEs have thousands of passage arrangements; thus, identifying an optimal arrangement is difficult. The heat transfer efficiency of PFHEs is another challenge for large-scale ASUs. The adaptability of TE to variable working conditions is important.

5.1 LPM of TE for variable working conditions

TE is an important equipment to generate cold energy and ensure the stable operation of cryogenic ASUs [37]. The refrigerating capacity of TE pertains to the external work during the expansion process, which is equal to the change in enthalpy of the fluid in the expansion process. The enthalpy drop increases correspondingly with the increase in expansion ratio, leading to the reduction of isentropic efficiency and waste of resources. Hence, TE design has strict requirements. With continuous technological development, the holdup of liquid in the expander increases gradually, and full-liquid TE is expected to be a developing trend in the future. Wang et al. [38] developed a cryogenic liquid turbine expander as a replacement for traditional Joule–Thomson valves used in cryogenic systems for energy saving. Yan et al. [39] studied a novel expander for organic Rankine cycle (i.e., variable expansion ratio rotary blade expander) that can adjust the expansion ratio by adjusting the opening angle of the outlet according to variable working conditions.

TE is made up of an expander and a supercharger. As shown in Fig. 6, the volume flow rate of the expander is greater than that of the supercharger. Given that they have the same rotation angular velocity, the impeller diameter of the former is larger than that of the latter. Figures 6(a) and 6(b) show the experiment on TE; Fig. 6(c) shows a TE structure. The left part is the expansion end, and the right part is the supercharging end; and Fig. 6(d) shows a simulated expansion process of TE.

The LPM of TE is as follows. The enthalpy drop of external power in TE is called the refrigerating capacity of the expander. Isentropic efficiency η_{s} can be defined as the ratio of actual specific enthalpy drop Δh_{act} to isentropic specific enthalpy drop Δh_{s} for the same inlet state and exit pressure.

$$\eta_{\mathrm{TE}} = \Delta h_{\mathrm{act}}/\Delta h_{\mathrm{s}}, \quad (13)$$

where η_{TE} is the isentropic efficiency of the TE, Δh_{act} is the actual specific enthalpy drops of the TE (unit: kJ/kg), and Δh_{s} is the theoretical specific enthalpy drops of the turbo expansion (unit: kJ/kg).

$$\Delta h_{\mathrm{act}} = h_{\mathrm{in}} - h_{\mathrm{out}}, \quad (14)$$

$$\Delta h_{\mathrm{s}} = h_{\mathrm{in}} - h_{\mathrm{out,s}}, \quad (15)$$

where h_{in} is the inlet specific enthalpy (unit: kJ/kg), h_{out} is the outlet specific enthalpy (unit: kJ/kg), and $h_{\mathrm{out,s}}$ is the theoretical outlet specific enthalpy (unit: kJ/kg).

For TE in the ASU refrigeration system, the actual refrigerating capacity (cooling power or cooling load) is more important than other features. The equation for the actual cooling capacity $\dot{Q}_{\mathrm{act}}$ of the TE is as follows:

$$\dot{Q}_{\mathrm{act}} = \dot{m}\Delta h_{\mathrm{act}} = \dot{m}\eta_{\mathrm{TE}}\Delta h_{\mathrm{s}}, \quad (16)$$

where $\dot{Q}_{\mathrm{act}}$ is the actual cooling capacity of the TE (unit: kW).

5.2 LPM of main PFHEs for variable working conditions

PFHE is the key equipment to realize heat exchange in condensation, liquefaction, and evaporation in cryogenic ASUs. The size of PFHEs increases with the increase in heat transfer load. This condition leads to an increase in the temperature difference between the cold and hot ends of PFHEs. The design of multi-stream PFHEs is complicated because of the different fin shapes, header structures, and passage arrangements [15], as shown in Fig. 7. The nonuniformity of the flow of multi-stream affects the heat transfer efficiency of PFHEs. Heat transfer enhancement

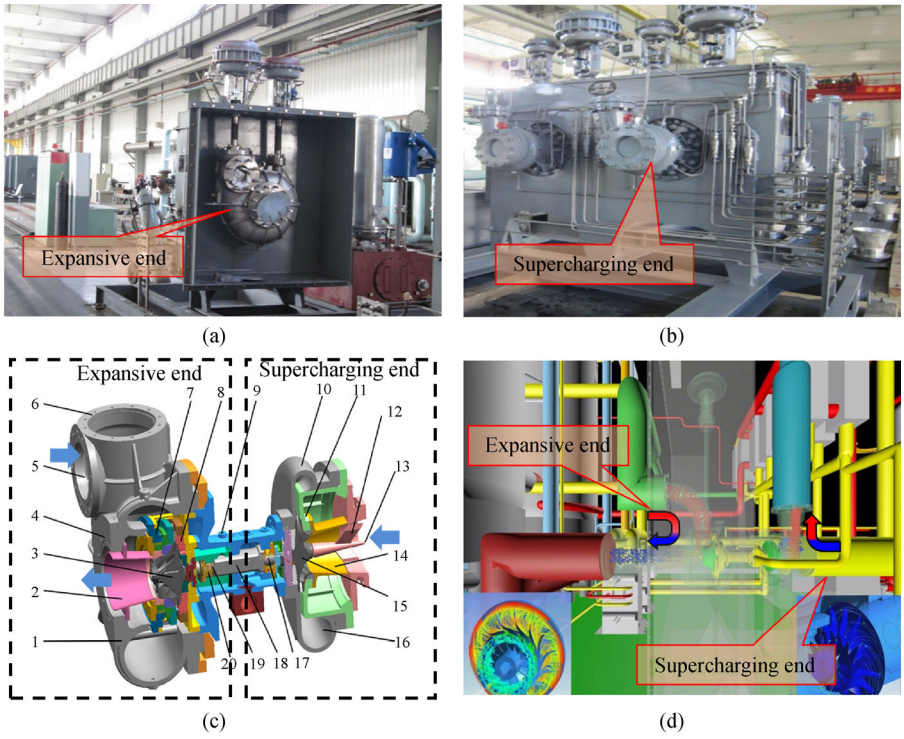

1–Expander casing; 2–Diffuser outlet; 3–Expander impeller; 4–Location to install expansion joint; 5–Expander inlet; 6–Location to install quick close valve; 7–Hold-down mechanism; 8–Inlet guide vane mechanism; 9–Bearing housing; 10–Booster casing; 11–Vaneless diffuser/diffuser guide vane; 12–Supercharger suction; 13–Fastening bolt; 14–Diffuser inlet; 15–Supercharger impeller/compressor; 16–Compressor casing; 17–Warm end outer bearing; 18–Main shaft/rotor; 19–Cold end inner bearing; 20–Labyrinth seal.

Fig. 6 TE. Experiment on TE: (a) Expansive end and (b) supercharging end. (c) TE structure. The left part is the expansive end, and the right part is the supercharging end. (d) Simulated flow process of TE.

generally increases flow resistance. Improving the heat transfer efficiency of PFHEs is the essential challenge in large-scale cryogenic ASUs.

Unsteady heat transfer has remarkable characteristics of small temperature difference, more than two streams, low allowable resistance, and drastic change in the physical properties of the multi-stream. Heat balance equations are set up in the direction of longitudinal and lateral heat transfer to realize high efficiency. On the basis of multiple dynamic equilibria, the temperature difference of the hot end is reduced from 4 to 2 K, and the total heat transfer coefficient is increased from 1958 to 2879 W/(m$^2\cdot$°C). The allowable design pressure is increased from 7.5 to 8.2 MPa.

The LPM of the main PFHEs is as follows. Heat transfer rate $\dot{Q}$, heat transfer efficiency ψ, and pressure drop $\Delta P_{\mathrm{PFHEs}}$ are the main factors affecting the performance of PFHEs and can be obtained with Eqs. (17)–(20).

(1) Heat transfer rate

$$\dot{Q} = UA_0\Delta T_{\mathrm{m}}, \tag{17}$$

where $\dot{Q}$ is the heat transfer rate (unit: kW), U is the overall heat transfer coefficient (unit: W/(m$^2\cdot$K^{-1})), A_0 is the total heat transfer surface area (unit: m^2), and ΔT_{m} is the mean temperature difference between streams (unit: K).

PFHEs have different flow patterns, such as counterflow, cross flow, cross-counterflow and co-current flow. Different flow patterns correspond to different ΔT_{m}, with counterflow as an example.

$$\Delta T_{\mathrm{m}} = [(T_{\mathrm{h,i}} - T_{\mathrm{c,o}}) - (T_{\mathrm{h,o}} - T_{\mathrm{c,i}})] \\ /\ln[(T_{\mathrm{h,i}} - T_{\mathrm{c,o}})/(T_{\mathrm{h,o}} - T_{\mathrm{c,i}})], \tag{18}$$

where $T_{\mathrm{h,i}}$ is the hot flow inlet temperature (unit: K), $T_{\mathrm{h,o}}$ is the hot flow outlet temperature (unit: K), $T_{\mathrm{c,o}}$ is the cold flow outlet temperature (unit: K), and $T_{\mathrm{c,i}}$ is the cold flow inlet temperature (unit: K).

(2) Heat transfer efficiency

Many formulas can be used to calculate the heat transfer efficiency of PFHEs. In this work, the calculation is based on the refrigerating capacity of the expander and the heat transfer rate of PFHEs.

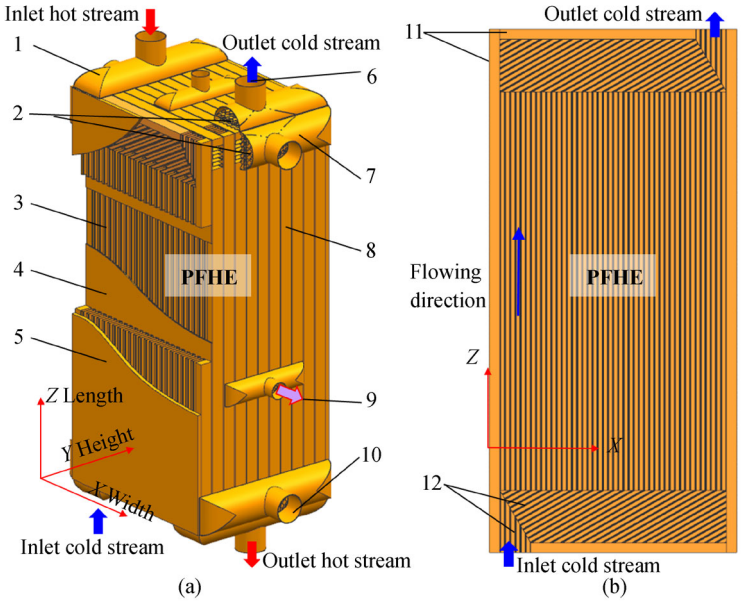

Fig. 7 Vertical brazed aluminum PFHE. (a) Overall structure of the PFHE; (b) a layer of passage.

$$\psi = \dot{Q}/\dot{Q}_{\text{act}}, \tag{19}$$

where ψ is the heat transfer efficiency.

(3) Pressure drop

By considering only the pressure drop caused by friction, it can be expressed as follows:

$$\Delta P_{\text{PFHEs}} = 2fL\dot{m}^2/(D_e\rho), \tag{20}$$

where ΔP_{PFHEs} is the pressure drop of PFHEs (unit: MPa), f is the friction factor, L is the heat exchanger length in Z direction (unit: m), and D_e is the equivalent diameter of the flowing passage (unit: m).

An operating flexibility increasing model is proposed based on the LPMs of TE and PFHEs. The temperature of the fluid diverted from the intermediate header is relatively high, whereas the temperature from the end header is low. The flexible operation can adjust not only the temperature of TE but also the working condition of the main PFHEs. The operation process can be divided into three stages to meet variable working conditions and increase operating flexibility:

(1) In the start-up stage, the $\dot{m}$ from end headers should be maximized to reduce the T_i of TE, and the $\dot{m}$ from intermediate headers should be minimized.

(2) When the critical point is reached, the T_i of TE is cold enough (about 164 K). At this time, the $\dot{m}$ from end headers should be reduced gradually, whereas the $\dot{m}$ from intermediate headers should be increased gradually.

(3) When the normal stable operating state is reached, the $\dot{m}$ from end headers should be minimized to maintain the T_i of TE, and the $\dot{m}$ from intermediate headers should be maximized.

6 LPM of the distillation process

The distillation process consists of two PCs (lower and upper columns). Distillation is the ultimate part of the air separation process. Separation of air occurs in the distillation process, and air is separated according to the boiling point of its different components. The design challenges of current PCs are low specific surface area and difficulty in achieving high flux. Predicting the liquid flooding of gas–liquid phases is also difficult.

6.1 LPM of PCs for variable working conditions

Distillation columns are the ultimate units used for separating air components in ASUs, and they are responsible for a large part of the total ASU inefficiency [40]. A distillation column mainly includes upper, lower, crude argon, and pure argon columns. The early form of the rectification column is the sieve tray column, which is simple and has low operating elasticity. To improve the energy efficiency of the continuous distillation process, the packed column gradually replaced the sieve tray column [41]. Under the same theoretical conditions, the resistance of the structured PC is about 10% of that of the sieve plate column due to the small resistance of the former. The advantage of reduced resistance lies in the fact that it can

be more energy saving. The operating load is affected by the sieve tray column liquid leakage and flooding velocity, whereas PC is influenced only by flooding velocity. PCs with high flux structured packing can be designed.

In the 100000 Nm^3 O_2/h large-scale ASU, the primary difficulty in the control of PCs stems from their nonlinear behavior, especially of columns producing high-purity gases [42]. The feedstock inside PCs are modeled and simulated to determine the flow state of the air inside by using DMU and CFD. Figure 8(a) presents a cold box that has distillation columns inside; Fig. 8(b) presents the CFD simulation process of the upper column; Fig. 8(c) presents a gas–liquid distributor; and Fig. 8(d) presents the flow state of the air in the PC.

The LPM of PC is as follows. With large-scale ASU development, PC design has become an important and complex process. Air separation occurs in the distillation column, and many mixtures are contained in it. The pressure drop of the distillation column is an important factor that affects distillation efficiency [43], and it can be calculated with Eqs. (21)–(29). The larger the pressure drop is, the more disadvantageous it is to air separation.

$$\nabla P_{\mathrm{irr}} = \nabla P_{\mathrm{d}}[(1-h_{\mathrm{l}}/\varepsilon)/(1-\varepsilon)]^{(2+C)/3}/(1-h_{\mathrm{l}}/\varepsilon)^{4.65}, \tag{21}$$

where

$$\nabla P_{\mathrm{d}} = 0.75 f_0 \left[(1-\varepsilon)/\varepsilon^{4.65}\right] \rho_{\mathrm{g}} u_{\mathrm{g}}^2 / d_{\mathrm{p}}, \tag{22}$$

$$h_{\mathrm{l}} = h_0 \left[1 + 20\left(\nabla P_{\mathrm{irr}}/(Z\rho_{\mathrm{l}} g)\right)^2\right], \tag{23}$$

$$h_0 = 0.555 Fr_{\mathrm{L}}^{1/3}, \tag{24}$$

$$Fr_{\mathrm{l}} = u_{\mathrm{l}}^2 \alpha_{\mathrm{p}}/(g\varepsilon^{4.65}), \tag{25}$$

$$f_0 = C_1/Re_{\mathrm{g}} + C_2/(Re_{\mathrm{g}}^{0.5}) + C_3, \tag{26}$$

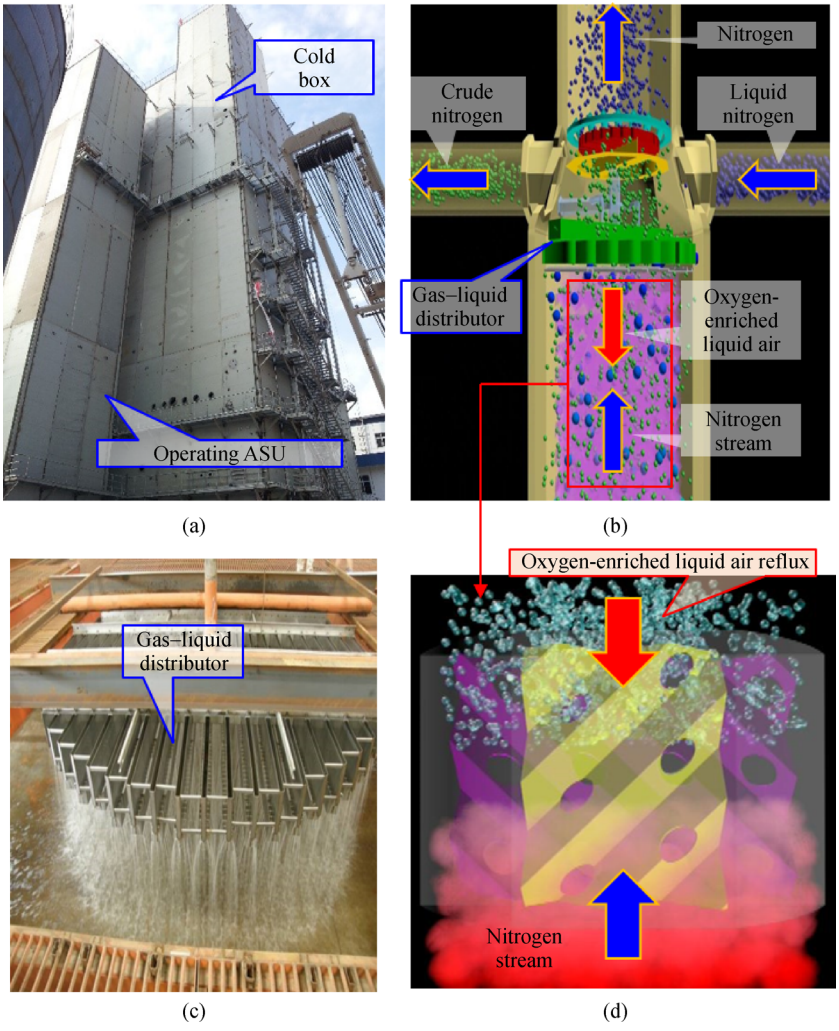

Fig. 8 Feedstock inside PCs. (a) Cold box; (b) CFD simulation process of the upper column; (c) gas–liquid distributor; (d) flow state of the air in PC.

$$Re_g = [6(1-\varepsilon)/\alpha_p]u_g\rho_g/\mu_g, \quad (27)$$

$$C = \left(-C_1/Re_g - C_2/(2Re_g^{0.5})\right)/f_0, \quad (28)$$

$$\alpha_p = 6(1-\varepsilon)/d_p, \quad (29)$$

where ∇P_{irr} is the pressure drop through an irrigated bed (unit: MPa), ∇P_d is the pressure drop through an unirrigated (dry) bed (unit: MPa), C_1, C_2, and C_3 are constants, ρ_l is liquid phase density (unit: kg/m^3), ρ_g is gas phase density (unit: kg/m^3), h_l is the liquid holdup of the PC, h_0 is the liquid holdup below the loading point, f_0 is the friction factor for flow past a single particle, g is gravitational acceleration (unit: m/s^2), Fr_l is the Froude number for liquid, Re_g is the Reynolds number for gas, Z is the total height of packing (unit: m), d_p is the particle diameter (m), α_p is the specific surface area of packing (unit: m^2/g), u_g is actual gas flow velocity (unit: m/s), and u_l is liquid flow velocity (unit: m/s).

Flooding refers to the accumulation of the liquid phase in the distillation column for various reasons, and it significantly reduces the efficiency of PC. The flooding point is crucial for PC dimensioning. In PC design, the packing factor of flooding point F_f must be determined, which can be obtained with Eq. (31). Flooding velocity u_f can be calculated with Eq. (32).

$$u_g = 4V_s/(\pi D^2), \quad (30)$$

$$F_f = u_g\rho_g^{0.5}, \quad (31)$$

$$u_f = F_f u_g, \quad (32)$$

where V_s is the volume flow rate of fluid under working conditions (unit: m^3/s), D is the diameter of PC (unit: m), F_f is the packing factor of the flooding point (unit: m$\cdot$s$^{-1}\cdot$(kg$\cdot$m^{-3})$^{0.5}$), and u_f is the flooding velocity (unit: m/s).

The degree ω of variable working condition of PC in ASU can be measured by percentage of gas when flooding point occurs with a certain liquid spray density.

6.2 Liquid holdup of PC for variable working conditions

Fluid flow in PC has been widely studied. Bradtmöller et al. [44] used X-ray computer tomography and light-induced fluorescence to investigate the morphology of liquid flow inside a structured PC and studied the effect of the variation in viscosity and liquid load. Kiss and Olujić [45] reviewed the development of heat exchange enhancement technology in rectifying columns. Chang et al. [46] proposed a structure of a full-tower ideal internal thermally coupled air separation column and presented a rigorous mathematic model and parameter analysis. The model has a strong driving force of heat transfer and large energy-saving potential.

The liquid holdup h_l of PC refers to the volume of liquid held by the surface and void of the packing layer per unit volume under given operating conditions. Liquid holdup can be divided into dynamic liquid holdup h_d and static liquid holdup h_s. h_d is the main component of total h_l. Its value is related not only to filler type, size, material, and liquid characteristics but also to liquid spray density. A comparison of fluid holdup between ω= 75% and ω= 105% load of PCs obtained by computed tomography is shown in Fig. 9.

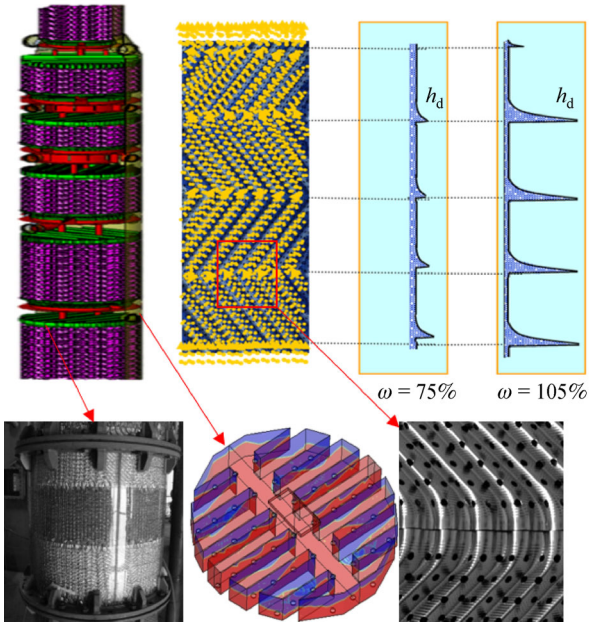

Fig. 9 Comparison of h_l between ω = 75% and ω = 105% PCs.

7 Design and experimental results of a large-scale cryogenic ASU using the LPM method

7.1 Comparison of experimental and theoretical physical properties of SCFs

The working properties in the stable state can be obtained according to the proposed method, and doing so is important to the design of ASUs. First, the physical properties of several special conditions were measured with the experimental method and compared with theoretical working parameters. Figure 10 presents an SCF experimental platform that can obtain the physical properties of SCFs via the combination of experimental and theoretical analyses.

Oxygen, nitrogen, and argon in air have a specific liquefaction temperature at a low-pressure state. The liquefaction temperature increases with the increase in

(a) (b)

Fig. 10 SCF experimental platforms for measuring physical properties. (a) Cryogenic fluid; (b) oscilloscope.

pressure until the pressure reaches the critical point. Oxygen, nitrogen, and argon are not liquefied again. Comparisons of experimental and theoretical critical physical properties of various components in ASUs are provided in Table 1. The difference between experimental and theoretical results is small, and the maximum relative error is 3.00%, which can be further reduced.

7.2 Complete cryogenic design for large-scale ASU using LPM

The challenges caused by the enlargement of cryogenic ASUs are considered, and the LPM method is used to optimize large-scale ASUs. The performance of AC, MSA, main PFHEs, and PC is obviously improved, as shown in Figs. 11 and 12.

Figure 11(a) presents the relationship between AC efficiency η_{AC} and atmosphere air mass flow rate $\dot{m}_{air}$. The theoretical curve can be exactly approximated using "rough first then precise" strategy by recursively reducing the interval ranges. With the increase in $\dot{m}_{air}$, η_{AC} increases gradually then decreases rapidly. The maximum initial value of η_{AC} is 86.72% when $\dot{m}_{air}$ is 188.86 kg/s. Under various working conditions, the mean initial value of η_{AC} is 71.98%. After the recursive optimization of the design, the mean efficiency is significantly improved with a ratio of 7%. The maximum optimized value of η_{AC} is 89.16% when $\dot{m}_{air}$ is 171.7 kg/s, and the mean optimized value of η_{AC} is 77.06%.

Figure 11(b) presents the relationship between the pressure drop of MSA ΔP_{MSA} and atmospheric air mass flow rate $\dot{m}_{air}$. As indicated in Fig. 11(a), with the increase in $\dot{m}_{air}$, ΔP_{MSA} continues to increase. Under various working conditions, the mean initial value of ΔP_{MSA} is 9.5975 kPa. After the recursive optimization of the design, ΔP_{MSA} becomes smaller than before with a ratio of 10.7%. The mean optimized value of ΔP_{MSA} is 8.5737 kPa.

Figure 12(a) presents the relationship between the main PFHEs' efficiency η_{PFHEs} and gaseous oxygen mass flow rate $\dot{m}_{O_2}$. As shown in Fig. 12(b), with the increase in $\dot{m}_{O_2}$, η_{PFHEs} increases gradually then decreases. The maximum initial value of η_{PFHEs} is 95.55% when $\dot{m}_{O_2}$ is 15.31 kg/s. Under various working conditions, the mean initial value of η_{PFHEs} is 86.78%. After the recursive optimization of the design, the mean efficiency is improved with a ratio of 1.9%. The maximum optimized value of η_{PFHEs} is 96.64% when $\dot{m}_{O_2}$ is 15.35 kg/s, and the mean optimized value of η_{PFHEs} is 88.40%.

Table 1 Comparisons of experimental and theoretical critical physical properties of various components in ASU

Components	Status	T_c /K	P_c /MPa	ρ_c /(kg·m^{-3})	C_p /(kJ·kg^{-1}·K^{-1})	μ /(Pa·s)	ν /(m^2·s^{-1})
Nitrogen (N_2)	Theoretical	126.19	3.3958	313.30	1.1239	5.4400×10^{-6}	1.7363×10^{-8}
	Experimental	125.32	3.4720	315.60	1.1527	5.3500×10^{-6}	1.7154×10^{-8}
Oxygen (O_2)	Theoretical	154.58	5.0430	436.16	1.6994	5.4437×10^{-6}	1.2481×10^{-8}
	Experimental	155.82	5.1020	437.36	1.7503	5.3639×10^{-6}	1.2583×10^{-8}
Argon (Ar)	Theoretical	150.69	4.8630	535.60	0.5658	7.1618×10^{-6}	1.3372×10^{-8}
	Experimental	150.31	4.9240	536.80	0.5762	7.1527×10^{-6}	1.3518×10^{-8}

Note: ν is the kinematic viscosity; C_p is the specific heat capacity at constant pressure; μ is the dynamic viscosity; T is the temperature; P is the pressure; ρ is the density; and the subscript "c" means critical.

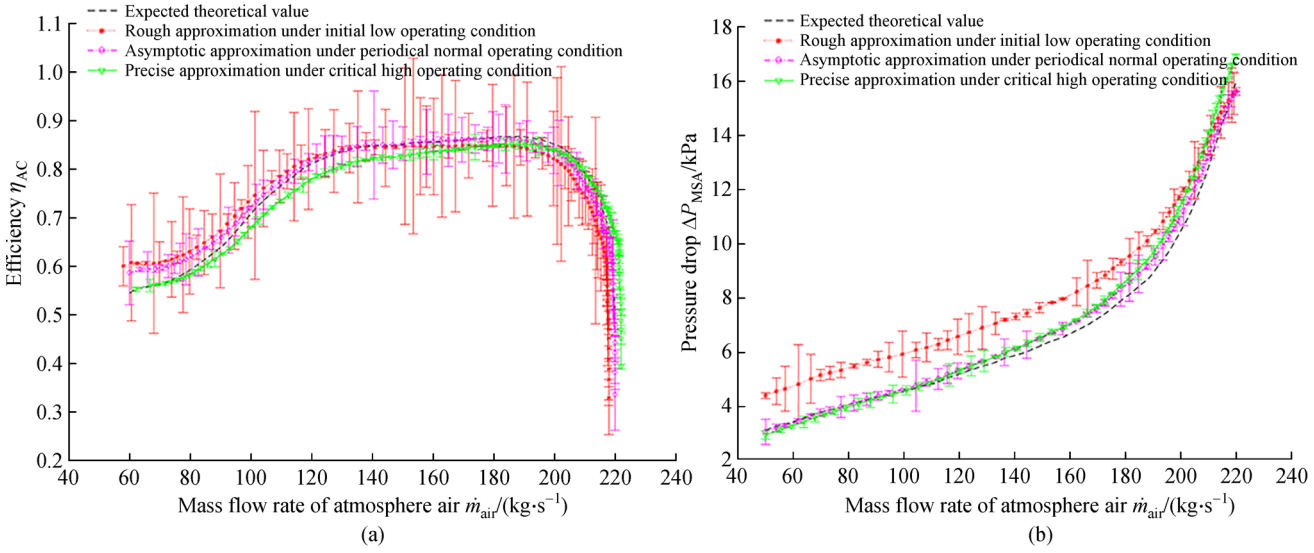

Fig. 11 (a) AC efficiency; (b) pressure drop of MSA.

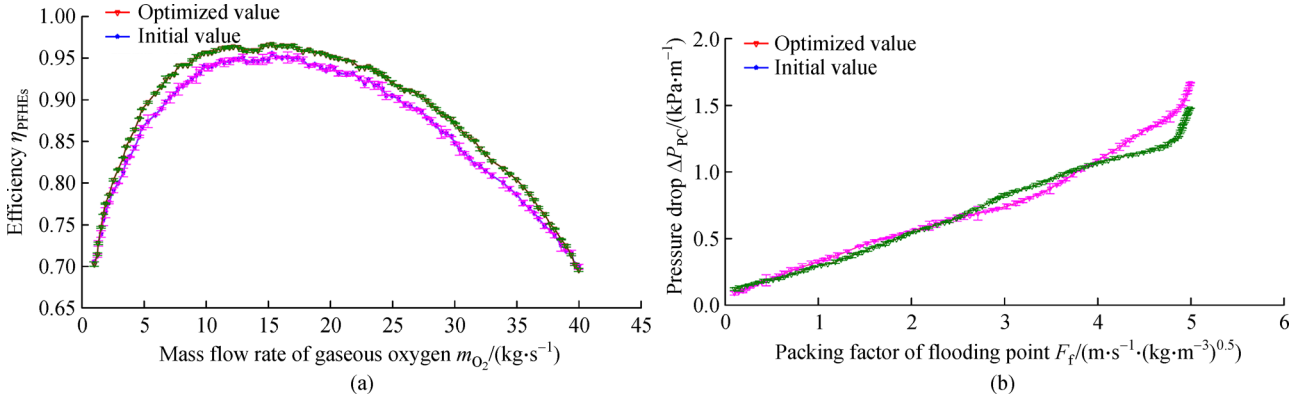

Fig. 12 (a) Main PFHEs' efficiency; (b) pressure drop of PC.

Figure 12(b) presents the relationship between the pressure drop of PC ΔP_{PC} and the packing factor of flooding point F. Figure 12(a) shows that with the increase in F_f, ΔP_{PC} continues to increase. Under various working conditions, the maximum initial value of ΔP_{PC} is 1.6693 kPa/m. After the recursive optimization of the design, the maximum ΔP_{PC} is decreased with a ratio of 11.4%. The maximum optimized value of ΔP_{PC} is 1.4782 kPa/m.

7.3 Experimental results using LPM

The LPM method is applied to the overall design of large-scale cryogenic ASUs and achieves remarkable results. The main oxygen products (in normal state) and parameters of the 100000 Nm^3 O_2/h large-scale ASU are listed in Table 2. The conditions of the ASU are as follows. The scale of the ASU is 100000 Nm^3/h, and the normal air intake is 507500 Nm^3/h. The operating conditions of large-scale cryogenic ASUs are complex and can be classified into multiple statuses, namely, low-load, normal-load, and overload conditions. The operating conditions can vary within 75% to 105% of normal conditions. The calculation error of the physical properties can be within 0.5%, the deviation of the flow resistance inhomogeneity at the large scale is below 1%, and the oxygen extraction rate of the structured PC is 99.9%. The purity of oxygen is 99.6% O_2, and the purity of nitrogen is 10 ppm O_2.

The 100000 Nm^3 O_2/h large-scale ASU produces qualified oxygen and nitrogen products successfully. It adopts internal compression and high automation technology, structured PC, and total rectification hydrogen-free argon production. A comparison of the results before and after using LPM in the 100000 Nm^3 O_2/h large-scale ASU is presented in Table 3. According to the challenge of the large-scale ASU, the corresponding overcoming approaches considerably improve the efficiency of the entire unit.

Table 2 Products and parameters of 100000 Nm^3 O_2/h large-scale ASU

Products and parameters	Minimum working condition/($Nm^3 \cdot h^{-1}$)	Designed working condition/($Nm^3 \cdot h^{-1}$)	Maximum working condition/($Nm^3 \cdot h^{-1}$)	Purity/ppm	Outlet pressure/MPa
High-pressure oxygen	75375	100500	106550	$\geqslant 9.96 \times 10^5$ O_2	5.9
High-pressure nitrogen	6850	6850	9250	$\leqslant 10$ O_2	7.0
Low-pressure nitrogen	69500	69500	78500	$\leqslant 10$ O_2	1.0
LOX	2500	1500	0	$\geqslant 9.96 \times 10^5$ O_2	–
LIN	2500	1000	0	$\leqslant 10$ O_2	–

Note: 1 ppm = 0.0001%= 1e–6.

Table 3 Comparison of results before and after using LPM in the 100000 Nm^3 O_2/h large-scale ASU

Processes	Units	Status	Performance parameters	Performance before using LPM	Performance after using LPM	Ratio
Adsorption process	AC	Axial flow type	Shaft power	$P_s = 26138$ kW	$P_s = 27561$ kW	5.44%
			Isentropic efficiency	$\eta_{AC} = 82.6\%$	$\eta_{AC} = 89.6\%$	8.47%
		Centrifugal type	Shaft power	$P_s = 12894$ kW	$P_s = 13195$ kW	2.33%
			Isentropic efficiency	$\eta_{AC} = 84.3\%$	$\eta_{AC} = 87.6\%$	3.91%
	MSA	Adsorption	Adsorption pressure drop	$\Delta P_{MSA} = 7.26$ kPa	$\Delta P_{MSA} = 6.79$ kPa	–6.47%
		Regeneration	Regeneration pressure drop	$\Delta P_{MSA} = 7.13$ kPa	$\Delta P_{MSA} = 6.74$ kPa	–5.47%
		Maximum	Maximum pressure drop	$\Delta P_{MSA} = 14.39$ kPa	$\Delta P_{MSA} = 13.53$ kPa	–5.98%
Heat transfer process	TE	Expansive end	Isentropic efficiency	$\eta_{TE} = 86\%$	$\eta_{TE} = 89\%$	3.49%
		Supercharging end	Isentropic efficiency	$\eta_{TE} = 81\%$	$\eta_{TE} = 82\%$	1.23%
	PFHEs	Whole	Isentropic efficiency	$\eta_{PFHEs} = 86.78\%$	$\eta_{PFHEs} = 88.40\%$	1.87%
			Total heat transfer coefficient	$U = 2286$ W/($m^2 \cdot$°C)	$U = 2518$ W/($m^2 \cdot$°C)	10.15%
			Heat transfer efficiency	$\psi = 87.6\%$	$\psi = 93.8\%$	7.08%
			Maximum Pressure drop	$\Delta P_{PFHEs} = 17$ kPa	$\Delta P_{PFHEs} = 16$ kPa	–5.88%
Distillation process	PC	Whole	Upper column Pressure drop	$\Delta P_{PC} = 3.6$ kPa	$\Delta P_{PC} = 3.4$ kPa	–5.56%
			Lower column Pressure drop	$\Delta P_{PC} = 4.3$ kPa	$\Delta P_{PC} = 4.1$ kPa	–4.65%

Note: P_s, shaft power of AC; η_{AC}, isentropic efficiency of the compressor; ΔP_{MSA}, pressure drop of MSA; η_{TE}, isentropic efficiency of the turbo expander; η_{PFHEs}, isentropic efficiency of PFHEs; ΔP_{PFHEs}, pressure drop of PFHEs; ΔP_{PC}, pressure drop of PC. Ratio =(Performance after using LPM–Performance before using LPM)/Performance before using LPM.

The total ASU net power consumption per unit of oxygen production is decreased from 0.523 to 0.49 kW/(Nm^3 O_2) with an optimal ratio of 6.45%.

8 Conclusions

(1) LPM method for large-scale ASUs

A cryogenic design method based on LPM for large-scale ASUs under a continuous process is proposed. The continuous process is decomposed top–down into adsorption, heat transfer, and distillation processes. The piece-wise-lumped parameters are extracted under variable working conditions using LPM on the basis of the material and energy flows within the continuous process. The LPM method can address the difficulty of correlating and coupling thousands of technical parameters in ASU.

(2) "Rough first then precise" modeling using T–S fuzzy interval detection

To improve the accuracy of the parameters extracted using LPM, a "rough first then precise" modeling method is proposed by expanding the feasible domain using fuzzy intervals. T–S fuzzy interval detection is recursively employed to approximate each stable state by using an

improved Gaussian membership function. Considering that the traditional method for variable working condition design of ASUs using a predefined uniform threshold cannot detect critical operating conditions adaptively, T–S fuzzy interval detection is recursively employed to determine whether the critical point is detected or not by using different thresholds. Compared with the traditional method, T–S fuzzy interval detection is suitable for the stable analysis of multi-stream coupling problems.

(3) Variable working condition design for 100000 Nm^3 O_2/h large-scale ASU

The 100000 Nm^3 O_2/h large-scale ASU is successfully designed using LPM. With LPM, the performance of AC, MSA, TE, main PFHEs, and PC in the ASU is enhanced to adapt to variable working conditions. The designed value of net power consumption per unit of oxygen production (kW/(Nm^3 O_2)) is decreased with an optimal ratio of 6.45%. The proposed method is useful for the top–down forward design of similar LSCSs.

Nomenclature

a_i, b_i, c_i	Parameter set of the shape-changing degree of the membership function
A_f	Total area of the hole (m^2)
C_p	Specific heat capacity at constant pressure ($J\cdot kg^{-1}\cdot K^{-1}$)
C_1, C_2, C_3	Constants
d	Bore diameter (m)
d_p	Particle diameter (m)
D	Diameter of PC (m)
D_e	Equivalent diameter of the flowing passage (m)
f	Friction factor
f_0	Friction factor for flow past a single particle
F_f	Packing factor of the flooding point ($m\cdot s^{-1}\cdot(kg\cdot m^{-3})^{0.5}$)
Fr_l	Froude number for liquid
g	Gravitational acceleration (m/s^2)
h	Specific enthalpy (J/kg)
Δh	Enthalpy drop (kJ/kg)
h_0	Liquid holdup below the loading point
h_d	Dynamic liquid holdup of the packing column
h_l	Liquid holdup of the packing column
h_s	Static liquid holdup of the packing column
H	Height of MSA (m)
k_1, k_2	Constants
L	Heat exchanger length (m)
$\dot{m}$	Fluid mass flow rate (kg/s)
N	Iteration number
ΔP	Pressure drop (MPa)
P_c	Critical pressure (MPa)
P_s	Shaft power of AC (kW)
$\dot{Q}$	Heat transfer rate (kW)
$\dot{Q}_{act}$	Actual cooling capacity of TE (kW)
Re_g	Reynolds number for the gas
S	State parameter set
T	Temperature of fluid (K)
T_c	Critical temperature (K)
ΔT_m	Mean temperature difference between streams (K)
u	Fluid flow speed (m/s)
u_f	Flooding velocity (m/s)
u_g	Actual gas flow velocity (m/s)
U	Overall heat transfer coefficient ($W\cdot m^{-2}\cdot K^{-1}$)
ν	Kinematic viscosity (m^2/s)
V_s	Volume flow rate of fluid under working conditions (m^3/s)
x	Input or variables in premise
y	Output of the model
Z	Total height of packing (m)
α_p	Specific surface area of packing (m^2/g)
β	Truncation error
γ	Compression ratio of the air compressor
ε	Porosity
η	Isentropic efficiency
λ_i	Fuzzy approximation error of ith judgement
μ	Dynamic viscosity (Pa·s)
ρ_l	Fluid density (kg/m^3)
ρ_c	Critical density (kg/m^3)
ψ	Heat transfer efficiency
ω	Degree of variable working condition of PC in ASU

Subscripts

AC	Air compressor
c	Cold streams
d	Unirrigated (dry) bed
EC	Evaporator condenser
g	Gas fluid
h	Hot streams
i	Inlet
irr	Irrigated bed
k	Known
l	Liquid fluid
LC	Lower column
MSA	molecular sieve adsorber
o	Outlet
PC	Packing column
PFHEs	Plate-fin heat exchangers

TE	Turbo expander
UC	Upper column

Acknowledgements This work was funded by the National Natural Science Foundation of China (Grant Nos. 51775494, 51821093, and 51935009), the National Key Research and Development Project (Grant No. 2018YFB1700701), and Zhejiang Key Research and Development Project (Grant No. 2019C01141).

References

1. Fu Q, Kansha Y, Song C, et al. A cryogenic air separation process based on self-heat recuperation for oxy-combustion plants. Applied Energy, 2016, 162: 1114–1121
2. Hashim S S, Mohamed A R, Bhatia S. Oxygen separation from air using ceramic-based membrane technology for sustainable fuel production and power generation. Renewable & Sustainable Energy Reviews, 2011, 15(2): 1284–1293
3. Smith A R, Klosek J. A review of air separation technologies and their integration with energy conversion processes. Fuel Processing Technology, 2001, 70(2): 115–134
4. Zhang W, Lu S, Ding X. Recent development on innovation design of reconfigurable mechanisms in China. Frontiers of Mechanical Engineering, 2019, 14(1): 15–20
5. Huang R, Zavala V M, Biegler L T. Advanced step nonlinear model predictive control for air separation units. Journal of Process Control, 2009, 19(4): 678–685
6. Kansha Y, Kishimoto A, Nakagawa T, et al. A novel cryogenic air separation process based on self-heat recuperation. Separation and Purification Technology, 2011, 77(3): 389–396
7. Fu Q, Zhu L, Chen X. Complete equation-oriented approach for process analysis and optimization of a cryogenic air separation unit. Industrial & Engineering Chemistry Research, 2015, 54(48): 12096–12107
8. Aneke M, Wang M. Potential for improving the energy efficiency of cryogenic air separation unit (ASU) using binary heat recovery cycles. Applied Thermal Engineering, 2015, 81: 223–231
9. Cao Y, Swartz C L E, Flores Cerrillo J, et al. Dynamic modeling and collocation-based model reduction of cryogenic air separation units. AIChE Journal. American Institute of Chemical Engineers, 2016, 62(5): 1602–1615
10. Ebrahimi A, Ziabasharhagh M. Optimal design and integration of a cryogenic air separation unit (ASU) with liquefied natural gas (LNG) as heat sink, thermodynamic and economic analyses. Energy, 2017, 126: 868–885
11. Rizk J, Nemer M, Clodic D. A real column design exergy optimization of a cryogenic air separation unit. Energy, 2012, 37(1): 417–429
12. Tong L, Zhang A, Li Y, et al. Exergy and energy analysis of a load regulation method of CVO of air separation unit. Applied Thermal Engineering, 2015, 80: 413–423
13. Jin B, Zhao H, Zheng C, et al. Control optimization to achieve energy-efficient operation of the air separation unit in oxy-fuel combustion power plants. Energy, 2018, 152: 313–321
14. Xu J H, Zhang S Y, Tan J R, et al. Multi-actuated mechanism design considering structure flexibility using correlated performance reinforcing. Journal of Zhejiang University. Science A: Applied Physics & Engineering, 2015, 16(11): 864–873
15. Xu J H, Chen X J, Zhang S Y, et al. Thermal design of large plate-fin heat exchanger for cryogenic air separation unit based on multiple dynamic equilibriums. Applied Thermal Engineering, 2017, 113: 774–790
16. Zhang S Y, Xu J H, Guo H W, et al. A research review on the key technologies of Intelligent design for customized products. Engineering, 2017, 3(5): 631–640
17. Xu J H, Wang T T, Zhang S Y, et al. Energy-efficient enhancement for viscoelastic injection rheomolding using hierarchy orthogonal optimization. Mathematical Problems in Engineering, 2018, 2018: 7054385
18. Abdo R F, Pedro H T C, Koury R N N, et al. Performance evaluation of various cryogenic energy storage systems. Energy, 2015, 90: 1024–1032
19. Karellas S, Schuster A, Leontaritis A D. Influence of supercritical ORC parameters on plate heat exchanger design. Applied Thermal Engineering, 2012, 33–34(1): 70–76
20. Son C H, Park S J. An experimental study on heat transfer and pressure drop characteristics of carbon dioxide during gas cooling process in a horizontal tube. International Journal of Refrigeration, 2006, 29(4): 539–546
21. Lisboa P F, Fernandes J, Simões P C, et al. Computational-fluid-dynamics study of a Kenics static mixer as a heat exchanger for supercritical carbon dioxide. Journal of Supercritical Fluids, 2010, 55(1): 107–115
22. Negoescu C C, Li Y, Al-Duri B, et al. Heat transfer behaviour of supercritical nitrogen in the large specific heat region flowing in a vertical tube. Energy, 2017, 134: 1096–1106
23. Avili M G, Sabet J K, Ghoreishi S M. Experimental characterization of a random packing with high specific surface area in a small diameter cryogenic distillation column. Progress in Nuclear Energy, 2018, 106: 417–424
24. Raman A S, Li H, Chiew Y C. Widom line, dynamical crossover, and percolation transition of supercritical oxygen via molecular dynamics simulations. Journal of Chemical Physics, 2018, 148(1): 014502
25. Lemmon E W, Tillner-Roth R. A Helmholtz energy equation of state for calculating the thermodynamic properties of fluid mixtures. Fluid Phase Equilibria, 1999, 165(1): 1–21
26. Zhu L, Garst M, Rosch A, et al. Universally diverging Gruneisen parameter and the magnetocaloric effect close to quantum critical points. Physical Review Letters, 2003, 91(6): 066404
27. Saha P, Sandilya P. A dynamic lumped parameter model of injection cooling system for liquid subcooling. International Journal of Thermal Sciences, 2018, 132: 552–557
28. Liu Q, Xu X. PID neural network control of a membrane structure inflation system. Frontiers of Mechanical Engineering, 2010, 5(4): 418–422
29. Takagi T, Sugeno M. Fuzzy identification of systems and its applications to modeling and control. Readings in Fuzzy Sets for Intelligent Systems, 1993, 15(1): 387–403
30. Škrjanc I, Blažič S, Agamennoni O. Identification of dynamical

systems with a robust interval fuzzy model. Automatica, 2005, 41(2): 327–332
31. Willems F, Heemels W P M H, de Jager B D, et al. Positive feedback stabilization of centrifugal compressor surge. Automatica, 2002, 38(2): 311–318
32. Semlitsch B, Mihăescu M. Flow phenomena leading to surge in a centrifugal compressor. Energy, 2016, 103(C): 572–587
33. Torrisi G, Grammatico S, Cortinovis A, et al. Model predictive approaches for active surge control in centrifugal compressors. IEEE Transactions on Control Systems Technology, 2016, 25(6): 1947–1960
34. Gravdahl J T, Egeland O, Vatland S O. Drive torque actuation in active surge control of centrifugal compressors. Automatica, 2002, 38(11): 1881–1893
35. Boinov K O, Lomonova E A, Vandenput A J A, et al. Surge control of the electrically driven centrifugal compressor. IEEE Transactions on Industry Applications, 2006, 42(6): 1523–1531
36. Rege S U, Yang R T, Buzanowski M A. Sorbents for air prepurification in air separation. Chemical Engineering Science, 2000, 55(21): 4827–4838
37. Niu L, Hou Y, Sun W, et al. The measurement of thermodynamic performance in cryogenic two-phase turbo-expander. Cryogenics, 2015, 70: 76–84
38. Wang K, Sun J, Song P. Experimental study of cryogenic liquid turbine expander with closed-loop liquefied nitrogen system. Cryogenics, 2015, 67: 4–14
39. Yan J, Han Y, Tian J, et al. Performance investigation of a novel expander coupling organic Rankine cycle: Variable expansion ratio rotary vane expander for variable working conditions. Applied Thermal Engineering, 2019, 152: 573–581
40. Van der Ham L V, Kjelstrup S. Improving the heat integration of distillation columns in a cryogenic air separation unit. Industrial & Engineering Chemistry Research, 2011, 50(15): 9324–9338
41. Bruinsma O S L, Krikken T, Cot J, et al. The structured heat integrated distillation column. Chemical Engineering Research & Design, 2012, 90(4): 458–470
42. Hwang Y L. On the nonlinear wave theory for dynamics of binary distillation columns. AIChE Journal. American Institute of Chemical Engineers, 1991, 37(5): 705–723
43. Stichlmair J, Bravo J L, Fair J R. General model for prediction of pressure drop and capacity of countercurrent gas/liquid packed columns. Gas Separation & Purification, 1989, 3(1): 19–28
44. Bradtmöller C, Janzen A, Crine M, et al. Influence of viscosity on liquid flow Inside structured packings. Industrial & Engineering Chemistry Research, 2015, 54(10): 2803–2815
45. Kiss A A, Olujić Ž. A review on process intensification in internally heat-integrated distillation columns. Chemical Engineering and Processing, 2014, 86: 125–144
46. Chang L, Liu X, Dai L, et al. Modeling, characteristic analysis, and optimization of ideal internal thermally coupled air separation columns. Industrial & Engineering Chemistry Research, 2012, 51(44): 14517–14524

Author Information

Jinghua XU, born in 1979, is currently an associate professor at Zhejiang University in China. He received his Ph.D. from Zhejiang University, China, in 2009. His research interests include mechanical design.
E-mail: xujh@zju.edu.cn

Tiantian WANG, born in 1995, is currently a Master's Degree candidate in Mechanical Engineering College, Zhejiang University, China. His research interests include CAD.
E-mail: 21725118@zju.edu.cn

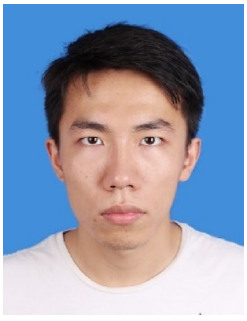

Qianyong CHEN, born in 1993, is currently a Ph.D. candidate in Mechanical Engineering College, Zhejiang University, China. His research interests include CAD.
E-mail: 11625067@zju.edu.cn

Shuyou ZHANG, born in 1963, is currently a professor at Zhejiang University, China. He received his Ph.D. from Zhejiang University, China, in 1999. His research interests include CAD/CG.
E-mail: zsy@zju.edu.cn

Jianrong TAN, born in 1954, is currently an academician in the Chinese Academy of Engineering and a professor in the Mechanical Engineering College of Zhejiang University, China. He received his Ph.D. from Zhejiang University, China, in 1992. His research interests include product design methodology.
E-mail: egi@zju.edu.cn